

Current sheets and pressure anisotropy in the reconnection exhaust

A. Le, J. Egedal, J. Ng, H. Karimabadi, J. Scudder, V. Roytershteyn, W. Daughton, and Y.-H. Liu

Citation: *Physics of Plasmas* (1994-present) **21**, 012103 (2014); doi: 10.1063/1.4861871

View online: <http://dx.doi.org/10.1063/1.4861871>

View Table of Contents: <http://scitation.aip.org/content/aip/journal/pop/21/1?ver=pdfcov>

Published by the [AIP Publishing](#)

Articles you may be interested in

[A review of pressure anisotropy caused by electron trapping in collisionless plasma, and its implications for magnetic reconnection](#)

Phys. Plasmas **20**, 061201 (2013); 10.1063/1.4811092

[The structure of the magnetic reconnection exhaust boundary](#)

Phys. Plasmas **19**, 022110 (2012); 10.1063/1.3685755

[The effects of strong temperature anisotropy on the kinetic structure of collisionless slow shocks and reconnection exhausts. I. Particle-in-cell simulations](#)


Phys. Plasmas **18**, 062110 (2011); 10.1063/1.3601760


[Model of electron pressure anisotropy in the electron diffusion region of collisionless magnetic reconnection](#)

Phys. Plasmas **17**, 122102 (2010); 10.1063/1.3521576


[Development and anisotropy of three-dimensional turbulence in a current sheet](#)

Phys. Plasmas **14**, 062304 (2007); 10.1063/1.2743518

A collection of five pieces of Pfeiffer Vacuum equipment, including a red turbopump, a silver turbopump, a silver backing pump, a red turbopump with a long shaft, and a silver chamber component.

 Vacuum Solutions from a Single Source

- Turbopumps
- Backing pumps
- Leak detectors
- Measurement and analysis equipment
- Chambers and components

PFEIFFER  **VACUUM**

Current sheets and pressure anisotropy in the reconnection exhaust

A. Le,¹ J. Egedal,² J. Ng,³ H. Karimabadi,¹ J. Scudder,⁴ V. Roytershteyn,¹ W. Daughton,⁵ and Y.-H. Liu⁵

¹*SciberQuest, Inc., Del Mar, California 92014, USA*

²*University of Wisconsin–Madison, Madison, Wisconsin 53706, USA*

³*PPPL, Princeton University, Princeton, New Jersey 08543, USA*

⁴*University of Iowa, Iowa City, Iowa 52242, USA*

⁵*Los Alamos National Laboratory, Los Alamos, New Mexico 87545, USA*

(Received 11 October 2013; accepted 23 December 2013; published online 14 January 2014)

A particle-in-cell simulation shows that the exhaust during anti-parallel reconnection in the collisionless regime contains a current sheet extending 100 inertial lengths from the X line. The current sheet is supported by electron pressure anisotropy near the X line and ion anisotropy farther downstream. Field-aligned electron currents flowing outside the magnetic separatrices feed the exhaust current sheet and generate the out-of-plane, or Hall, magnetic field. Existing models based on different mechanisms for each particle species provide good estimates for the levels of pressure anisotropy. The ion anisotropy, which is strong enough to reach the firehose instability threshold, is also important for overall force balance. It reduces the outflow speed of the plasma. © 2014 AIP Publishing LLC. [<http://dx.doi.org/10.1063/1.4861871>]

I. INTRODUCTION

Magnetic reconnection releases magnetic stress and energizes plasma in a range of astrophysical and laboratory environments.¹ A variety of numerical models—including resistive MHD, Hall-MHD, two-fluid, hybrid, and fully kinetic codes—have been used to study how anti-parallel reconnection occurs.²

Here, we use a particle-in-cell (PIC) simulation run to late times to assess the structure of the reconnection exhaust in the collisionless limit, which is the suitable regime for typical space plasmas. We find that the exhaust contains a current sheet extending $100d_i$ from the X line. The current sheet is composed of two sections: an inner electron layer dominated by electron currents and an outer layer that includes important ion kinetic effects. The electron current sheet near the X line is similar to ones observed in a number of previous simulations.^{3–5} The electron layer is coupled to the larger ion current sheet by electron parallel currents that flow along the outside of the magnetic separatrices. These currents at the exhaust boundary generate the out-of-plane magnetic field, the Hall field characteristic of kinetic reconnection.^{6,7} These features are indicated schematically in Fig. 1(b).

For comparison, a sketch of the Petschek model of reconnection⁸ is included in Fig. 1(a). In the Petschek model, which is based on resistive MHD with isotropic pressure, switch-off shocks form outside a small non-ideal region and are responsible for most of the acceleration and heating of the plasma. There have been isolated reports of slow shock-like features observed in the geotail,^{9,10} and the Petschek picture has been used to interpret observations in the solar wind.¹¹

The magnetic field geometry and current structures in the exhaust current sheet of our simulation, however, are not consistent with the Petschek model. One reason the Petschek model fails here is that the magnetic geometry contains gradients below ion kinetic scales, and the exhaust therefore lies

outside the scope of MHD. This is believed to be a typical feature of fast reconnection in collisionless plasmas.¹² In the sharply curved magnetic field lines of the exhaust, ions undergo bouncing Speiser orbits^{13,14} that alter the plasma properties and the current profile.¹⁵ It was found in previous hybrid simulations that $\sim 100d_i$ from the X line the exhaust is wide enough that the magnetic field gradients are on the order of an ion gyroradius,¹⁶ and generalized MHD-like shock analyses may be more suitable downstream of this region.¹⁷

We focus here on the current sheets that form in the exhaust within $100d_i$ from the X line. Previous hybrid^{15,16} and kinetic¹⁷ simulations found peaked current profiles within the region of ion bouncing orbits. The Speiser and other types of particle orbits in a reconnection geometry lead to complex velocity space distributions of both the electrons¹⁸ and the ions.¹⁴ Nevertheless, we find that most of the features of the central current sheet in the exhaust may be associated with one main kinetic effect, namely, the development of pressure anisotropy.^{19,20} During magnetospheric reconnection, pressure anisotropy has been observed in the electrons and the ions.^{21–24}

Pressure anisotropy reaching the firehose instability threshold is in fact uniquely capable of supporting very long, quasi-steady current sheets with a normal component of magnetic field.^{25–27} Mechanisms for generating anisotropy with a higher temperature parallel to the magnetic field have been proposed, and they are different for the electrons^{28,29} and the ions.³⁰ Furthermore, we find that the ion anisotropy contributes substantially to momentum balance of the entire exhaust. The pressure anisotropy is of comparable importance to the ion inertia, and it reduces the outflow speed of the plasma.

In the following sections, we describe the features of the ion and electron current sheets, emphasizing the important role of pressure anisotropy. The results are organized as follows: In Sec. II, we present the PIC simulation. Some details about the electron current sheet are given in Sec. III, and the

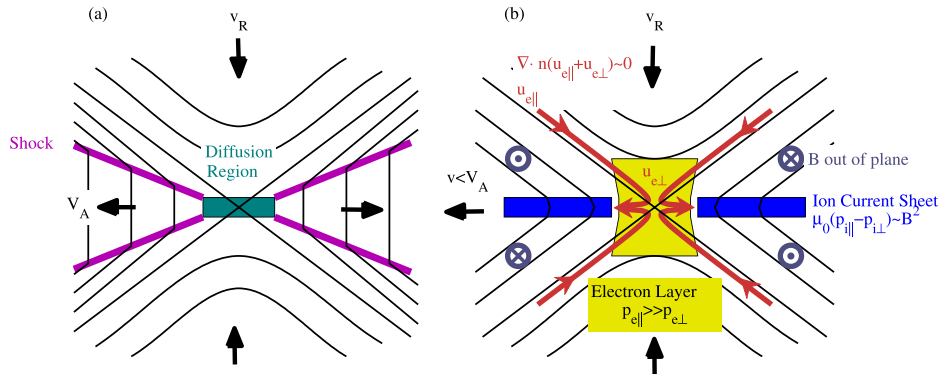


FIG. 1. Comparison of Petschek model and collisionless reconnection exhaust. (a) Sketch of the reconnection exhaust of the Petschek model. A pair of switch-off shocks bounds the exhaust outside of a non-ideal diffusion region. (b) Electron and ion current sheets form in the reconnection exhaust of a PIC simulation. They are supported by pressure anisotropy. In a region near the X line, the electrons are heated by an effective potential due to the parallel electric field as in Ref. 28. Parallel electron currents just outside the separatrices generate an out-of-plane magnetic field. The ions are heated by a mechanism described in Ref. 30.

ion current sheet is described in Sec. IV. In these sections, we review the models for the generation of pressure anisotropy and note how their predictions apply to the structure of the current sheets. Force balance and a related generalized Walen condition³¹ are discussed in Sec. V, followed by the Summary (Sec. VI).

II. EXHAUST IN A PIC SIMULATION OF ANTI-PARALLEL RECONNECTION

Our PIC simulation of reconnection begins from a Harris equilibrium without guide field. The focus here is on the structure of the reconnection exhaust well after the initial onset of tearing. We use a fairly large domain of $400d_i \times 100d_i = 10240 \text{ cells} \times 2560 \text{ cells}$ that allows the exhaust to fully develop without spurious boundary effects, which are further minimized by employing open boundary conditions appropriate for reconnection.³² There are $\sim 10^{10}$ numerical particles of each species. The 2D run uses a coordinate system with the out-of-plane y direction ignorable and the initial unperturbed magnetic field given by $B_x = B_0 \tanh(z/d_i)$, where $d_i = c/\omega_{pi}$ is the ion inertial length based on the peak Harris density n_0 . This simulation used the following parameters: mass ratio $m_i/m_e = 50$, initial uniform temperatures satisfying $T_{e0}/T_{i0} = 1$, $\omega_{pe}/\omega_{ce} = 2$, and background density $n_b = 0.5n_0$. With these parameters the upstream total (ion plus electron) $\beta = 0.5$.

Magnetic field profiles at $t = 225/\omega_{ci}$ are plotted in Fig. 2. The magnetic field strength B in Fig. 2(a) remains quite low in the center of the exhaust where the initial neutral sheet was located. The reconnecting field component B_x in Fig. 2(b) has a region of high shear at the center of the exhaust. This shear is produced by the out-of-plane current J_y plotted in Fig. 3(a), which exhibits a peaked current sheet that extends over $100d_i$ from the X line in either direction. This configuration is in contrast to the Petschek model, for example, in which the reversal of the magnetic field and hence, the peaks in the out-of-plane current occur in shocks located near the exhaust boundary. The reconnecting field is not “switched off” in the exhaust, but rather it gradually reverses direction with the sharpest change located in the central current sheet, consistent with previous simulations.¹⁷

The out-of-plane field B_y is plotted in Fig. 2(c). It is called the Hall field⁷ because it is generated by electron currents that flow when the ions and electrons decouple on small scales $\lesssim d_i$. In the fully developed reconnection exhaust, however, the out-of-plane magnetic field is neither confined to a small region near the X line nor to the vicinity of the magnetic separatrices. The field B_y extends hundreds of d_i and is significant throughout most of the region between the separatrices and the center of the exhaust. The quadrupolar structure of the out-of-plane field B_y , thus, fills an exhaust region much larger than any length scales typically associated with Hall physics.

It is mostly x (outflow) directed current that generates the out-of-plane magnetic field B_y . The current density J_x is plotted in Fig. 3(b). The current $J_x \sim (1/\mu_0)\partial B_y/\partial z$ is peaked both along the separatrices and in the center of the exhaust, producing the steeper gradients in B_y at both those locations. The current along the separatrices is mostly a parallel current carried by electrons. The current in the exhaust center, meanwhile, is largely a perpendicular current

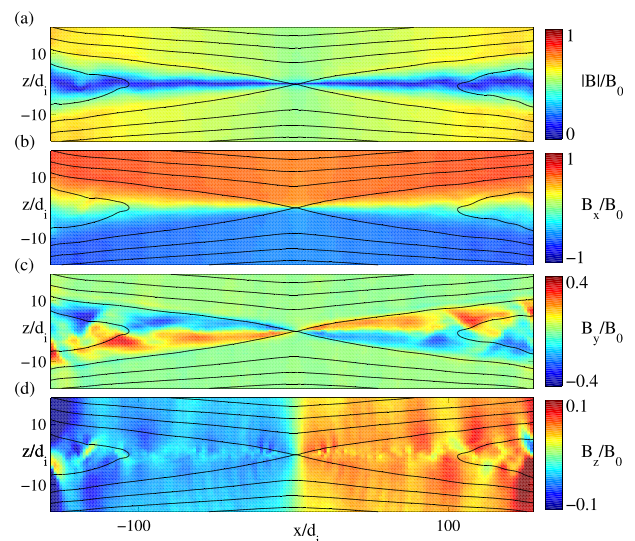


FIG. 2. Magnetic field profiles at time $t = 225/\omega_{ci}$ in a PIC simulation with sample in-plane field lines. (a) Magnetic field strength $|B|$, (b) reconnecting component B_x , (c) out-of-plane field B_y , and (d) reconnected field B_z .

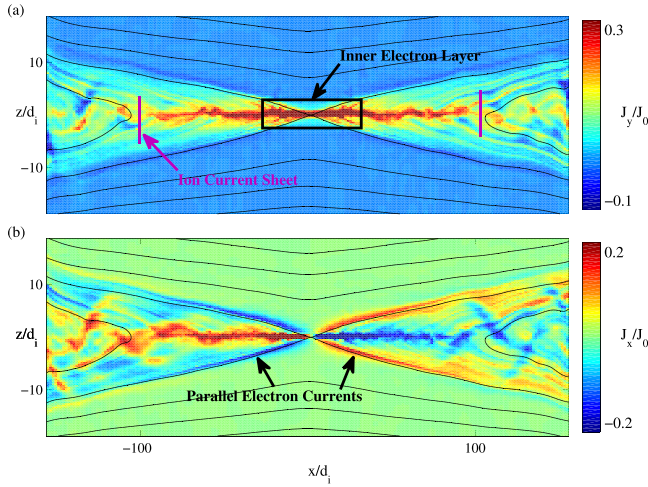


FIG. 3. Current density profiles. (a) Out-of-plane current density current J_y with the electron and ion sections of the current sheet labeled. (b) Outflow current density J_x . Parallel return currents (labeled) flow along the outside of the separatrix.

supported by electron pressure anisotropy very near the X line and ion anisotropy out to $\sim 100d_i$. The details are described in Secs. III–VI.

III. ELECTRON CURRENT SHEET

Next, we examine how the currents and exhaust geometry are related to the electron and ion dynamics. Near the X line, there is a sharply peaked electron current sheet $\sim 150d_e$ long and $\sim 3d_e$ wide that includes jets of electrons streaming out from the X line near the electron thermal speed. Similar current sheets have been observed in a number of previous PIC studies of anti-parallel reconnection.^{3,4,32} Electron current sheets are not limited to the anti-parallel limit, however, and modified types can become even longer at moderate guide fields.^{5,33} Most of the features of the electron current sheet are described by a model derived previously.²⁷ Some key points and details of this particular simulation are reviewed below.

The exhaust electron current sheet has been shown to develop due to electron pressure anisotropy immediately upstream of the exhaust,^{18,27} which allows a flux of perpendicular momentum into the electron jets. The main physical mechanism responsible for generating the anisotropy is particle trapping and acceleration by an electric field parallel to the magnetic field. The effect is parametrized by the acceleration potential Φ_{\parallel} ,^{28,29} which is the maximum energy acquired from the parallel electric field by an electron streaming along a magnetic field line. As seen in Fig. 4(a), the acceleration potential reaches $e\Phi_{\parallel}/T_{e0} \sim 2$ in the inflow region, and it typically becomes much larger in low $\beta_{e\infty}$ plasmas. Trapping in the potential leads to a characteristic electron distribution, such as the one plotted in Fig. 4(f), which is elongated in the parallel ($\sim v_x$) direction and has been observed during magnetospheric reconnection.³⁴ Note that within the electron current sheet, the electrons are not magnetized. Pitch angle mixing then leads to nearly isotropic flattop distributions^{35,36} farther downstream, like the one plotted in Fig. 4(e).

The parallel heating by Φ_{\parallel} leads to electron temperature anisotropy with the ratio $p_{e\parallel}/p_{e\perp}$ peaking at ~ 2 , as shown in Fig. 4(b). Downstream in the exhaust, on the other hand, the flattop distributions result in a nearly isotropic electron pressure.^{5,36,37} As seen in previous simulations, the electron pressure anisotropy supports the jet of out-flowing electrons near the X line by balancing the $\mathbf{J} \times \mathbf{B}$ force on the cross-field electron current, which is plotted in Fig. 4(c). In particular, around the region of sharply curved magnetic field lines, the magnetic tension $\mathbf{B}\mathbf{B}/\mu_0$ and anisotropic pressure $(p_{e\parallel} - p_{e\perp})\hat{\mathbf{b}}\hat{\mathbf{b}}$ approximately balance. The electrons immediately outside the layer of current, thus, approach the firehose instability threshold $p_{e\parallel} - p_{e\perp} - B^2/\mu_0 = 0$.

While the electron pressure anisotropy determines the net current in the electron sheet, a fully kinetic treatment is required to determine the local electron current density profile.¹⁸ Meanwhile, in regions where the electrons are magnetized, the perpendicular electron flow is approximately

$$\mathbf{u}_{e\perp} \sim \frac{\mathbf{E} \times \mathbf{B}}{B^2} - \frac{1}{neB} \hat{\mathbf{b}} \times [\nabla p_{e\perp} + (p_{e\parallel} - p_{e\perp})\mathbf{K}], \quad (1)$$

where $\mathbf{K} = \hat{\mathbf{b}} \cdot \nabla \hat{\mathbf{b}}$ is the magnetic curvature vector. In general, the $\mathbf{E} \times \mathbf{B}$ and pressure gradient contributions to the divergence of the perpendicular electron flux need not cancel, $\nabla \cdot n\mathbf{u}_{e\perp} \neq 0$. Quasi-steady electron continuity is then

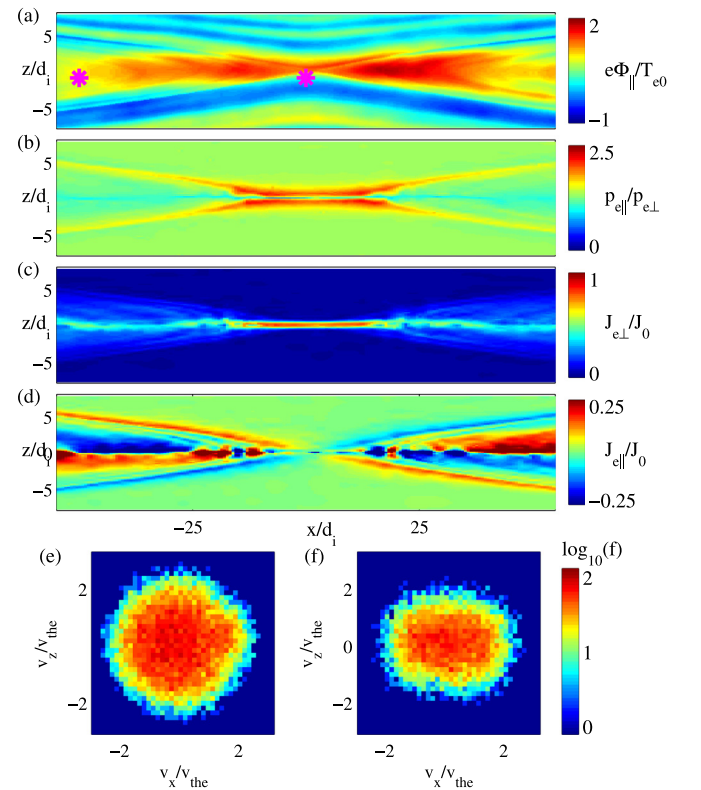


FIG. 4. An (a) acceleration potential Φ_{\parallel} induces (b) electron pressure anisotropy $p_{e\parallel}/p_{e\perp} > 1$. This sustains (c) a sheet of perpendicular electron current $J_{e\perp}$, whose divergence is canceled by (d) parallel electron currents $J_{e\parallel}$ just outside the magnetic separatrix. (Currents normalized to $J_0 = n_0 e v_{A0}$, where $v_{A0} = B_0 / \sqrt{\mu_0 n_0 m_i}$.) At the points marked by *'s in (a), the reduced electron distributions $f(v_x, v_z)$ are (e) a flattop distribution in the exhaust and (f) an elongated distribution with trapping²⁸ in the inflow.

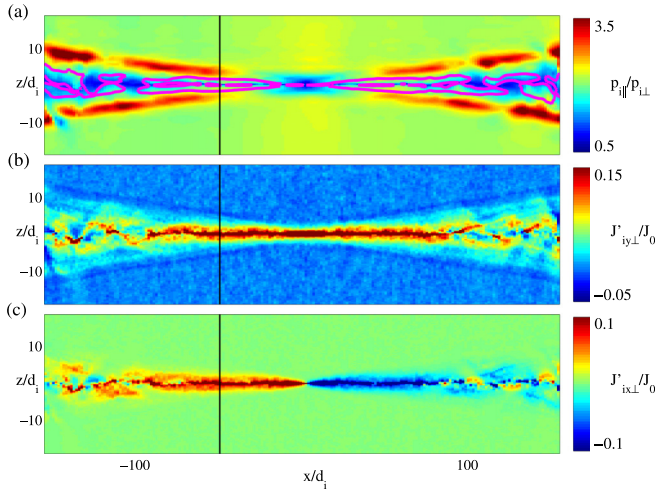


FIG. 5. (a) Ion pressure anisotropy with $p_{\parallel}/p_{\perp} > 1$ develops. The magenta contour indicates where the ions reach the firehose threshold $p_{\parallel} - p_{\perp} - B^2/\mu_0 = 0$. The (b) out-of-plane y and (c) outflow x components of the perpendicular ion current with the local $\mathbf{E} \times \mathbf{B}$ velocity subtracted, $\mathbf{J}_{\perp} = ne[\mathbf{u}_{i\perp} - (\mathbf{E} \times \mathbf{B})/B^2]$.

maintained by electron return currents flowing parallel to the magnetic field^{33,38} such that

$$\nabla \cdot n(\mathbf{u}_{e\perp} + \mathbf{u}_{e\parallel}) \sim 0. \quad (2)$$

The parallel electron current $nu_{e\parallel} = \hat{\mathbf{b}} \cdot n\mathbf{u}_e$ is plotted in Fig. 4(d). Note the peaked parallel current outside the magnetic separatrices, which consists of electrons flowing towards the X line to supply the current for the electron jets.

The channel of parallel electron current flowing along the separatrices generates the out-of-plane magnetic field component. This so-called Hall field requires the separation of ion and electron dynamics on small scales.⁶ Including only the Hall term itself, the magnetic field remains frozen into the electron flow, which is equivalent to retaining only

the $\mathbf{E} \times \mathbf{B}$ drift in Eq. (1).^{19,20} In the collisionless regime, however, the anisotropic electron pressure gradients dominate in allowing the strong perpendicular electron current near the X line.

IV. ION CURRENT SHEET

A surprising result is that the ions support a continuation of the current sheet. The enhanced current layer in the center of the reconnection exhaust extends out past $100d_i$ on both sides of the X line, as visible in Figs. 2(e) and 2(f). This is several times longer than the electron layer, which falls off by $25d_i$ (and is typically much shorter in simulations at more realistic mass ratios^{5,39}). In addition, the ion current sheet is supported by pressure anisotropy in a manner similar to the electron current sheet, although a different mechanism generates the anisotropy of each species. The ion pressure anisotropy is plotted in Fig. 5(a), and it reaches $p_{\parallel}/p_{\perp} \sim 4$. Here, p_{\perp} is an average over the two perpendicular directions, and the ion pressure anisotropy⁴⁰ peaks at $2|p_{i\perp 1} - p_{i\perp 2}|/(p_{i\perp 1} + p_{i\perp 2}) \sim 0.4$.

An existing model gives good estimates for the ion pressure anisotropy.^{30,41} The model accounts for two populations of ions in the exhaust,⁴² one streaming in from the inflow region and the other already accelerated in the field reversal region at the exhaust's center. Such counter-streaming ion beams have been observed in association with solar wind reconnection.⁴³ The two populations of ions are visible in the reduced ion distribution functions $f(v_x, v_z)$, which are summed over the out-of-plane velocity component, in Figs. 6(f) and 6(g). They are computed from the numerical particles contained in $0.1d_i$ squares centered at the points marked in Fig. 6(a). The beams in the exhaust are visible near the separatrices downstream from the X line. The ion beams are not strongly separated from the bulk ion population; with the beam's drift speed in this case is only around twice the ion thermal speed.

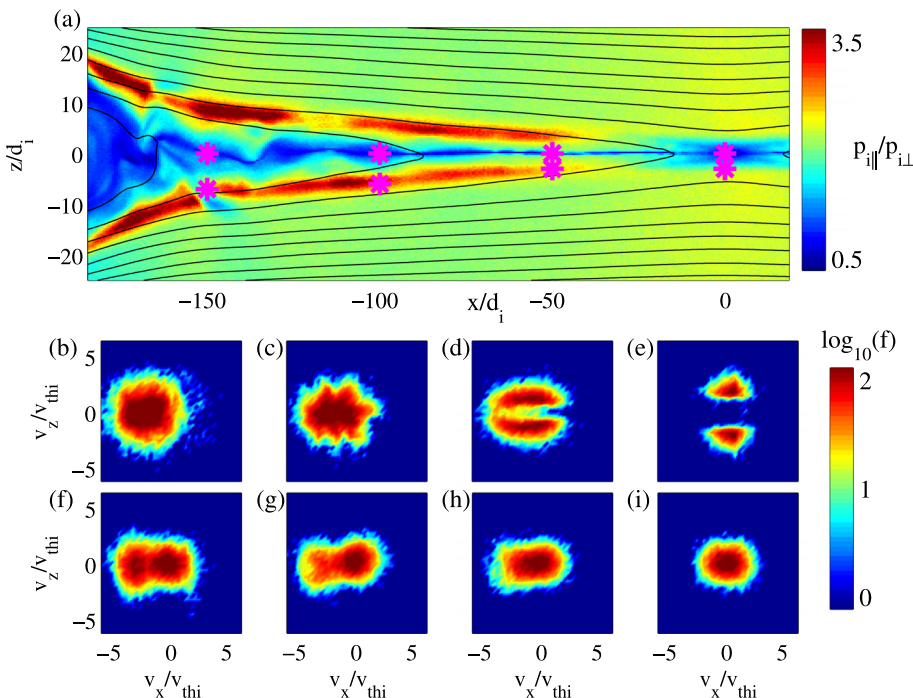


FIG. 6. (a) Ion pressure anisotropy in the exhaust. The reduced ion distributions $f(v_x, v_z)$ at the locations marked by *'s are plotted in (b)–(i).

In the exhaust center beyond the current sheet, the ion distributions look thermalized [Figs. 6(b) and 6(c)]. As pointed out in Ref. 16, the ion orbits in this region are chaotic because the field line radius of curvature is comparable to the ion gyroradius.⁴⁴ As a result, pitch angle mixing leads to a more isotropic distribution. The ion distributions in Figs. 6(d) and 6(e) within the ion current sheet contain counter-streaming ion beams. These form as a result of the Speiser bouncing motion of ions across the field reversal near the X line. It is interesting to note that similar features form in the electron distributions in the electron diffusion region, where there is a separation of upward- and downward-moving electron populations undergoing bouncing orbits.¹⁸ Further details of the ion distributions, including multiple classes of Speiser ions, have been found in recent numerical work.¹⁴

As far as the fluid picture of the reconnection exhaust is concerned, a main result of the ion kinetic behavior is the development of pressure anisotropy with $p_{i\parallel} > p_{i\perp}$. Including contributions from both the ions streaming in from the inflow and the ions that have already undergone bouncing motion yields estimates for the ion temperatures³⁰ of

$$T_{i\parallel} \sim m_i v_0^2 \frac{B_{x0}^2}{B_{xy}^2}, \quad T_{i\perp} \sim \frac{1}{2} m_i v_0^2 \frac{B_{y0}^2}{B_{xy}^2}, \quad (3)$$

where $v_0 = -E_y/B_z$ is the velocity of the de Hoffman-Teller frame, B_{x0} is evaluated outside the separatrix, B_{y0} is the typical peak out-of-plane field, and $B_{xy} = \sqrt{B_{x0}^2 + B_{y0}^2}$. These estimates agree well with the observed ion temperature, which increase in the exhaust by $\Delta T_{i\parallel}/T_{i0} \sim 1$ and $\Delta T_{i\perp}/T_{i0} \sim 0.8$. Note that this ion model includes an important effect of the out-of-plane magnetic field B_y , which generated along the separatrices mainly by parallel electron currents, and thus couples the electron and ion current dynamics.

To see that this model applies for the entire duration of the quasi-steady stage of reconnection, the total ion

temperature $T_i = (T_{i\parallel} + 2T_{i\perp})/3$ is plotted in Fig. 7(b) over the course of the simulation along the cut $50d_i$ from the X line. For reference, the reconnection rate E_y is plotted in Fig. 7(a). Beyond $t \sim 100/\omega_{ci}$, the general features do not depend on the time slice used, although the peak temperature tapers off the upstream magnetic flux is depleted. The ion temperature at the center of the exhaust is plotted in Fig. 7(c). It falls off as the upstream reconnecting field B_x^2 lowers, and the change in ion temperature ΔT_i is approximately proportional to the upstream Alfvén speed squared v_{Ax}^2 . The thermalization of cold ion beams in an Alfvénic outflow is one model consistent with this correlation.

The ion pressure anisotropy produced by the picking up and mixing of ion beams is strong enough to reach (and exceed) the firehose instability threshold, $p_{i\parallel} - p_{i\perp} - B^2/\mu_0 = 0$. The magenta contour in Fig. 5(a) shows where the ion firehose condition is met. As mentioned in Sec. III, this threshold is also the criterion for the formation of an extended current sheet, and the ion pressure anisotropy supports a sheet of perpendicular current. The out-of-plane (y) and outflow (x) components of the ion perpendicular current in the local $\mathbf{E} \times \mathbf{B}$ frame are plotted in Figs. 5(b) and 5(c). Note that for the positively charged ions, this flow is opposite the ambient exhaust velocity, and the ion pressure anisotropy therefore reduces the ion bulk outflow speed. This is opposed to the electron jets near the X line, which flow out faster than the local $\mathbf{E} \times \mathbf{B}$ speed.

While the ion current sheet is supported by pressure anisotropy like the electron sheet, there are some notable differences. The peak ion current density is ≥ 10 weaker than the peak electron current density near the X line. This is in part because the ion sheet is $\sim 2d_i$ wide, which is several times wider than the electron sheet. Additionally, in the external plasma rest frame, the electron current density is of a similar magnitude to the ion current density. In contrast, the electron current sheet near the X line is carried almost entirely by the electrons. In addition to pressure gradient-supported currents,

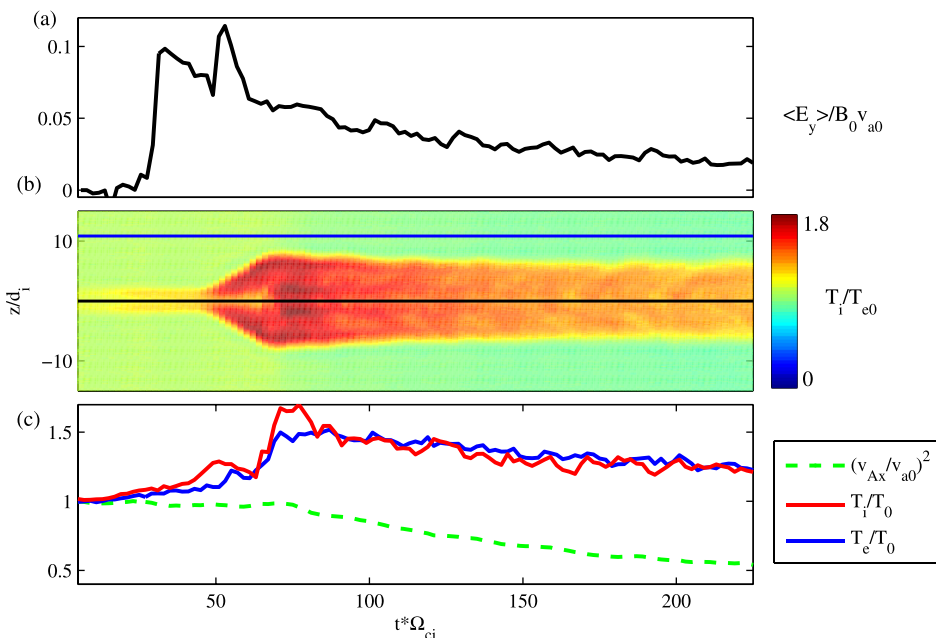


FIG. 7. (a) Reconnection rate $\langle E_y \rangle / B_0 v_{a0}$ over time, where $\langle E_y \rangle$ is an average over a square $\sim 3d_i$ wide centered on the X line. (b) Ion temperature $(T_{i\parallel} + 2T_{i\perp})/3$ along the cut $50d_i$ to the left of the X line over the course of the simulation. (c) The ion temperature T_i and electron temperature T_e at the center of the exhaust along with the upstream Alfvén speed squared based on the reconnecting field $v_{Ax}^2 = B_x^2/\mu_0 n m_i$.

a substantial portion of the electron current in the ion-scale layer is induced by $\mathbf{E} \times \mathbf{B}$ electron drifts on small scales over which the ions are unmagnetized.

V. FORCE BALANCE AND THE GENERALIZED WALEN CONDITION

Here, we examine how pressure anisotropy fits into force balance in the reconnection exhaust. For force balance across the exhaust in the z direction, gradients in z dominate, and

$$\frac{d}{dz} \left(p_{\perp} + \frac{B^2}{2\mu_0} \right) \sim 0. \quad (4)$$

This implies that the exhaust settles into a near-equilibrium such that the total pressure $p_{\perp} + B^2/2\mu_0$ is approximately uniform across any cut. The example cut of Fig. 8 through the exhaust is used to plot the main contributions to pressure balance in Fig. 9. The magnetic field strength gradually dips in the exhaust, and the magnetic pressure $B^2/2\mu_0$ (blue line) decreases. This is compensated by the plasma perpendicular pressure $p_{\perp} = p_{i\perp} + p_{e\perp}$ to yield a roughly uniform total pressure (red line).

Given that force balance across the exhaust current follows essentially from a 1D MHD-like condition, it is

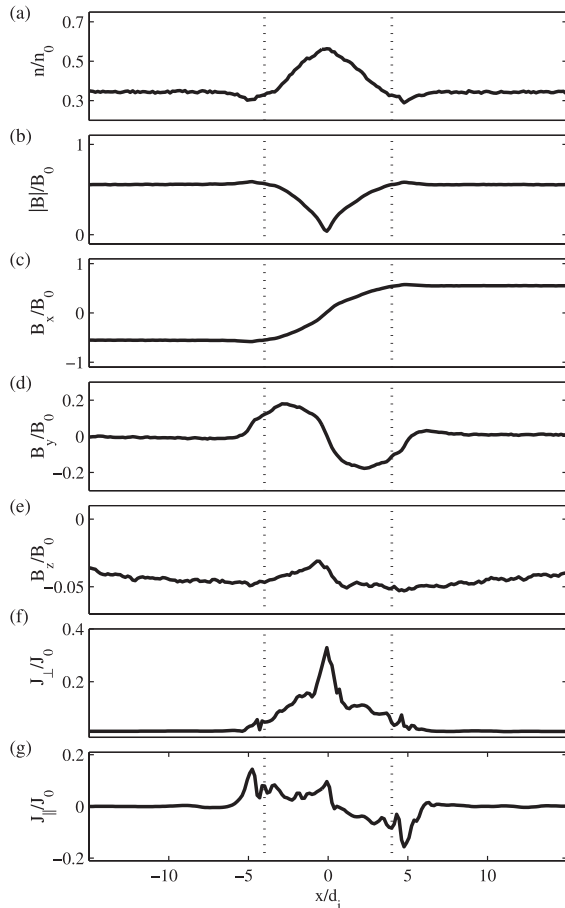


FIG. 8. Magnetic field and current density profiles along a vertical cut $50d_i$ from the X line (cuts marked in Fig. 5). Vertical dashed lines mark the magnetic separatrices.

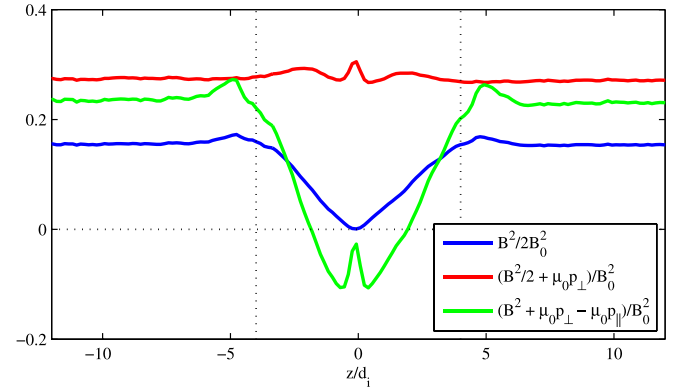


FIG. 9. (a) Pressure balance across the current sheet. Magnetic pressure $B^2/2\mu_0$, pressure $B^2/2\mu_0 + p_{\perp}$, and tension $p_{\parallel} - p_{\perp} - B^2/\mu_0$ along a vertical cut $50d_i$ from the X line. The firehose threshold is reached where the total tension (green) dips below zero.

reasonable to explore whether a similar treatment accounts for force balance in the outflow (x) direction. The 1D MHD conservation equations yield the set of Rankine-Hugoniot shock jump conditions,^{45,46} which in turn provide predictions for the reconnection exhaust in shock-based models such as the one of Petschek⁸ and its modification when pressure anisotropy is included.¹⁷ For example, a jump condition analysis results in the Walen relation, which predicts the following relationship between the magnetic field and plasma flow:⁴⁷

$$\mathbf{V}_w = \pm \sqrt{\frac{\rho_0}{\mu_0}} \left[\frac{\mathbf{B}}{\rho} - \frac{\mathbf{B}_0}{\rho_0} \right], \quad (5)$$

where the upstream pressure has been assumed isotropic. This holds for a discontinuity with an inflow speed equal to an upstream Alfvénic speed $u_z \sim B_z/\sqrt{\mu_0\rho_0}$ based on the normal magnetic field component, and it applies to rotational discontinuities and the switch-off shocks of the Petschek model.

In Fig. 10(a), the Walen relation prediction (red) for the ion outflow is compared to the direct PIC result (blue) along the cut used in Fig. 8. The same quantities are plotted for the out-of-plane direction in Fig. 10(b). While the Walen condition gives a rough estimate for the outflow speed in the reconnection exhaust, it is not satisfied very precisely. This is similar to observational data from a survey of magnetopause measurements, where the typical outflow speed was overestimated by the Walen condition by nearly a factor of two.⁴⁸

As noted above, the shock analysis is not expected to hold in this kinetic regime, where gradient scales in the exhaust are shorter than the ion gyroradius and an MHD shock transition would be roughly on the same scale as the exhaust itself.⁴⁹ A generalized Walen relation was proposed³¹ to handle cases like this where the ions are not magnetized and the plasma may carry large currents. The basic result (which follows from Eqs. (16) and (18) of Ref. 31) for a proton-electron plasma is that the electron flow, rather than the center of mass flow, should follow the Walen relation as stated in Eq. (5). The electron drifts are plotted in Fig. 10. Unlike the ions, the electrons continue to be nearly frozen

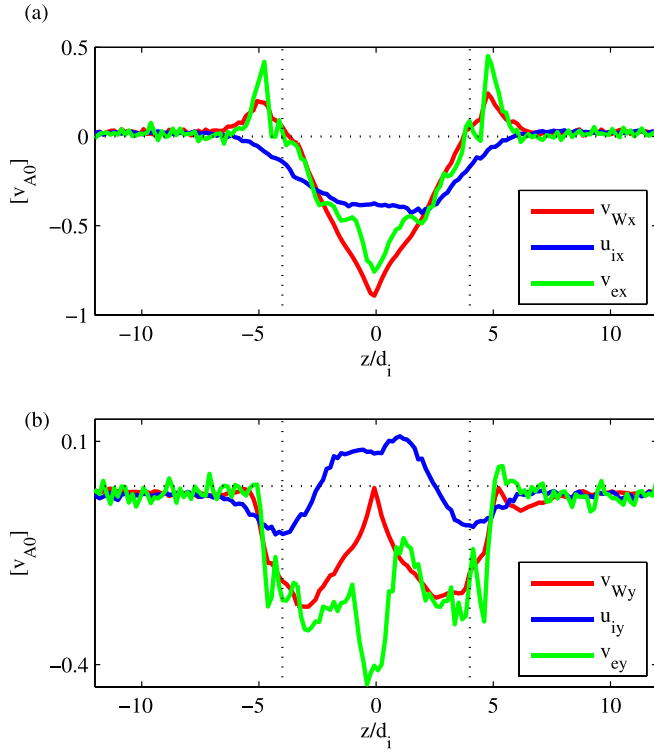


FIG. 10. The Walen relation (red) provides a good estimate for the electron flow (green) but it overestimates the ion flow (blue) by around a factor of 2. Near the separatrices (located at vertical dashed lines) and in a narrow channel at the exhaust's center, the electron Walen relation fails due to electron agyrotropy and other kinetic effects.

into the magnetic field, and their flow therefore rotates with the magnetic field. The predicted electron flow matches very well with the simulation results. The only substantial deviations of the electron flow from the Walen relation occur near the separatrices and in a narrow section at the exhaust's center, where the electrons are known to become agyrotropic,²³

reaching a maximum agyrotropy of $2|p_{e\perp 1} - p_{e\perp 2}|/(p_{e\perp 1} + p_{e\perp 2}) \sim 0.1$ at the center of the cut. The generalized Walen condition thus provides one diagnostic that may be useful in studying the exhaust current sheet in observational data.

Because a simple 1D analysis fails to quantify the various contributions to momentum balance in the outflow direction, we resort to calculating them directly from the simulation for a section of the exhaust bounded by the magnetic separatrix and a cutoff $100d_i$ from the X line [region marked in Fig. 11(a)]. In a quasi-steady state, the net x momentum flux \mathbf{T} across the boundary must be zero, where the flux \mathbf{T} is

$$\mathbf{T} = nm_i \mathbf{u}_i \mathbf{u}_i + \left(p_{\perp} + \frac{B^2}{2\mu_0} \right) \mathbf{I} + \left(p_{\parallel} - p_{\perp} - \frac{B^2}{\mu_0} \right) \hat{\mathbf{b}} \hat{\mathbf{b}} + \Pi. \quad (6)$$

Electron inertia has been neglected, and Π represents the non-gyrotropic part of the plasma pressure tensor. The contributions from the magnetic tension $\mathbf{B}\mathbf{B}/\mu_0$, magnetic pressure $B^2/2\mu_0$, plasma perpendicular pressure p_{\perp} , anisotropic pressure $p_{\parallel} - p_{\perp}$, and ion inertia $nm_i \mathbf{u}_i \mathbf{u}_i$ are plotted in Fig. 11 over the course of the simulation until time $t = 175/\omega_{ci}$. Note that because the separatrix is along the magnetic field, the magnetic tension and pressure anisotropy $(p_{\parallel} - p_{\perp} - B^2/\mu_0) \hat{\mathbf{b}} \hat{\mathbf{b}}$ only contribute along the boundary's vertical cut-off at $x = -100d_i$. The general results that follow are not sensitive to the choice of cut-off as long as it lies in the ion current sheet, or roughly 40 to $110d_i$ from the X line.

In Fig. 11, we consider x (outflow) momentum balance

$$0 \sim \oint (\hat{\mathbf{x}} \cdot \mathbf{T} \cdot \mathbf{n}) dl. \quad (7)$$

After an initial transient phase, the current sheet reaches a quasi-steady state in which the relative contributions to momentum balance plotted in Fig. 11(b) are roughly constant in

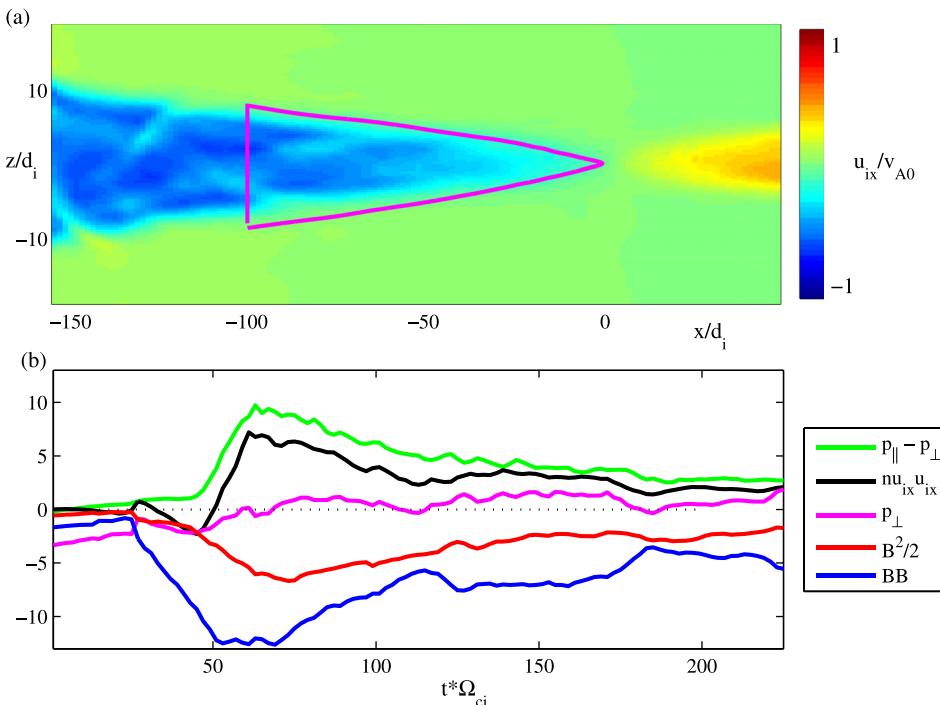


FIG. 11. (a) The magenta contour bounds a region bordered by the magnetic separatrix and extending $100d_i$ from the X line at time $t * \omega_{ci} = 225$. (b) The leading contributions to the loop integral for integrated x force balance over time.

time. The largest term is the magnetic tension \mathbf{BB}/μ_0 , which is the magnetic force driving reconnection. This force accelerates the plasma exhaust, and a large portion goes into the momentum flux carried by the plasma outflow $nm_i\mathbf{u}_i\mathbf{u}_i$. Meanwhile, a similar (and in this case even slightly greater) portion of the magnetic tension force is balanced by the anisotropic pressure $(p_{\parallel} - p_{\perp})\hat{\mathbf{b}}\hat{\mathbf{b}}$, which is predominantly ion anisotropy at the $100d_i$ cut-off.

In other words, the ion pressure anisotropy cancels around half of the magnetic tension force driving the outflow of plasma, thereby reducing the plasma exhaust speed. The pressure anisotropy therefore plays a large role in regulating the net flow of exhaust plasma.

VI. SUMMARY

A large PIC simulation of anti-parallel reconnection run to a late stage with open boundary conditions demonstrates the formation of electron and ion current sheets in the reconnection exhaust. The electron and ion structures are coupled by electron return currents that flow outside the separatrices along the magnetic field and generate the out-of-plane magnetic field. Recent simulations show that in 3D systems the electron current layers are unstable and break apart into filaments or flux ropes, leading to turbulent dynamics.⁵⁰ It is an open question whether the ion-scale current sheets are similarly susceptible to secondary instabilities that could lead to larger-scale turbulence over longer time scales in natural reconnection events.

The current sheets are supported by pressure anisotropy, an important feature in the dynamics of collisionless plasmas. The long, nearly steady current sheets require pressure anisotropy that approaches the firehose instability threshold. While the electron and ion current sheets are both supported by pressure anisotropy, the anisotropy is generated by different mechanisms for each species. The electrons are trapped and heated by a parallel electric field in the inflow region near the X line. In the anti-parallel case examined here, the electrons pitch angle mix in the weak magnetic field near the X line, and the exhaust distributions become nearly isotropic flattop distributions. The ions, on the other hand, form beams as they are picked up by the reconnection exhaust. This process generates pressure anisotropy throughout the exhaust.

Besides supporting a current sheet near the field reversal, the ion pressure anisotropy is important for the overall momentum balance of the exhaust. The pressure anisotropy balances a portion of the magnetic tension that accelerates the outflow. Based on the model for ion heating, which involves ion beams drifting at nearly the Alfvén speed, the importance of ion pressure anisotropy should be comparable to that of the ion inertia in a broad range of regimes.

Finally, in the region of the exhaust containing the ion current sheet, the gradient length scales are too small for MHD shock conditions to be applied. The Walén relation, for example, overestimates the outflow speed of the ions. Meanwhile, a generalized Walén condition holds to a good approximation for the electrons across a large portion of the exhaust, suggesting that the electron Walén condition will be a useful tool when coupled with magnetic field and

high-resolution electron measurements of collisionless reconnection in space.

ACKNOWLEDGMENTS

The work of A.L. and H.K.'s was supported by NASA Grant NNH11CC65C. J.E. acknowledges support through NASA Grant NNX10AL11G and NSF Grant Nos. ATM0802380 and OCI 0904734. J.S. acknowledges NSF Grant AGS-1153817 and NASA Grant NNX13AG08G. W.D.'s work was supported by the NASA Heliophysics Theory Program and the LDRD program at Los Alamos. Simulations were performed on Kraken provided by NSF at NICS and on Pleiades provided by NASA's HEC Program.

¹E. Priest and T. Forbes, *Magnetic Reconnection* (Cambridge University Press, 2000).

²J. Birn, J. F. Drake, M. A. Shay, B. N. Rogers, R. E. Denton, M. Hesse, M. Kuznetsova, Z. W. Ma, A. Bhattacharjee, A. Otto *et al.*, *J. Geophys. Res.* **106**, 3715, doi:10.1029/1999JA900449 (2001).

³H. Karimabadi, W. Daughton, and J. Scudder, *Geophys. Res. Lett.* **34**, L13104, doi:10.1029/2007GL030306 (2007).

⁴M. A. Shay, J. F. Drake, and M. Swisdak, *Phys. Rev. Lett.* **99**, 155002 (2007).

⁵A. Le, J. Egedal, O. Ohia, W. Daughton, H. Karimabadi, and V. S. Lukin, *Phys. Rev. Lett.* **110**, 135004 (2013).

⁶B. U. Ö. Sonnerup, *Magnetic Field Reconnection, in Solar System Plasma Physics*, edited by L. T. Lanzerotti, C. F. Kennel, and E. N. Parker (North-Holland, New York, 1979), Vol. 3, pp. 45–108.

⁷J. F. Drake, M. A. Shay, and M. Swisdak, *Phys. Plasmas* **15**, 042306 (2008).

⁸H. E. Petschek, NASA [Spec. Publ.] SP **50**, 425 (1964).

⁹Y. Saito, T. Mukai, T. Terasawa, A. Nishida, S. Machida, M. Hirahara, K. Maezawa, S. Kokubun, and T. Yamamoto, *J. Geophys. Res.* **100**, 23567, doi:10.1029/95JA01675 (1995).

¹⁰J. Seon, L. A. Frank, W. R. Paterson, J. D. Scudder, F. V. Coroniti, S. Kokubun, and T. Yamamoto, *J. Geophys. Res.: Space Phys.* **101**, 27383 (1996).

¹¹J. Gosling, S. Eriksson, R. Skoug, D. McComas, and R. Forsyth, *Astrophys. J.* **644**, 613 (2006).

¹²W. Daughton, V. Roytershteyn, B. J. Albright, H. Karimabadi, L. Yin, and K. J. Bowers, *Phys. Rev. Lett.* **103**, 065004 (2009).

¹³T. Speiser, *J. Geophys. Res.* **70**, 4219, doi:10.1029/JZ070i017p04219 (1965).

¹⁴S. Zenitani, I. Shinohara, T. Nagai, and T. Wada, *Phys. Plasmas* **20**, 092120 (2013).

¹⁵R.-F. Lottermoser, M. Scholer, and A. P. Matthews, *J. Geophys. Res.* **103**, 4547, doi:10.1029/97JA01872 (1998).

¹⁶K. Higashimori and M. Hoshino, *J. Geophys. Res.* **117**, A01220, doi:10.1029/2011JA016817 (2012).

¹⁷Y.-H. Liu, J. F. Drake, and M. Swisdak, *Phys. Plasmas* **19**, 022110 (2012).

¹⁸J. Ng, J. Egedal, A. Le, W. Daughton, and L. J. Chen, *Phys. Rev. Lett.* **106**, 065002 (2011).

¹⁹V. M. Vasyliunas, *Rev. Geophys.* **13**, 303, doi:10.1029/RG013i001p00303 (1975).

²⁰J. D. Scudder, *Space Sci. Rev.* **80**, 235 (1997).

²¹M. Oieroset, R. Lin, and T. Phan, *Phys. Rev. Lett.* **89**, 195001 (2002).

²²L.-J. Chen *et al.*, *J. Geophys. Res.* **113**, A12213, doi:10.1029/2008JA013385 (2008).

²³J. D. Scudder, R. D. Holdaway, W. S. Daughton, H. Karimabadi, V. Roytershteyn, C. T. Russell, and J. Y. Lopez, *Phys. Rev. Lett.* **108**, 225005 (2012).

²⁴T. D. Phan, G. Paschmann, C. Twitty, F. S. Mozer, J. T. Gosling, J. P. Eastwood, M. Oieroset, H. Rème, and E. A. Lucek, *Geophys. Res. Lett.* **34**, L14104, doi:10.1029/2007GL030343 (2007).

²⁵S. W. H. Cowley, *Planet. Space Sci.* **26**, 1037 (1978).

²⁶F. J. Rich, V. M. Vasyliunas, and R. A. Wolf, *J. Geophys. Res.* **77**, 4670 (1972).

²⁷A. Le, J. Egedal, W. Daughton, J. F. Drake, W. Fox, and N. Katz, *Geophys. Res. Lett.* **37**, L03106, doi:10.1029/2009GL041941 (2010).

- ²⁸J. Egedal, W. Fox, N. Katz, M. Porkolab, M. Oieroset, R. P. Lin, W. Daughton, and J. F. Drake, *J. Geophys. Res.* **113**, A12207, doi:10.1029/2008JA013520 (2008).
- ²⁹J. Egedal, A. Le, and W. Daughton, *Phys. Plasmas* **20**, 061201 (2013).
- ³⁰J. F. Drake, M. Swisdak, T. D. Phan, P. A. Cassak, M. A. Shay, S. T. Lepri, R. P. Lin, E. Quataert, and T. H. Zurbuchen, *J. Geophys. Res. (Space Phys.)* **114**, A051111, doi:10.1029/2008JA013701 (2009).
- ³¹J. D. Scudder, P. A. Puhl-Quinn, F. S. Mozer, K. W. Ogilvie, and C. T. Russell, *J. Geophys. Res.* **104**, 19817, doi:10.1029/1999JA900146 (1999).
- ³²W. Daughton, J. Scudder, and H. Karimabadi, *Phys. Plasmas* **13**, 072101 (2006).
- ³³O. Ohia, J. Egedal, V. S. Lukin, W. Daughton, and A. Le, *Phys. Rev. Lett.* **109**, 115004 (2012).
- ³⁴J. Egedal, M. Oieroset, W. Fox, and R. P. Lin, *Phys. Rev. Lett.* **94**, 025006 (2005).
- ³⁵Y. Asano *et al.*, *J. Geophys. Res.* **113**, A01207, doi:10.1029/2007JA012461 (2008).
- ³⁶J. Egedal, A. Le, N. Katz, L. J. Chen, B. Lefebvre, W. Daughton, and A. Fazakerley, *J. Geophys. Res.* **115**, A03214, doi:10.1029/2009JA014650 (2010).
- ³⁷L. J. Chen, A. Bhattacharjee, P. A. Puhl-Quinn, H. Yang, N. Bessho, S. Imada, S. Muehlbachler, P. W. Daly, B. Lefebvre, Y. Khotyaintsev *et al.*, *Nat. Phys.* **4**, 19 (2008).
- ³⁸A. Le, J. Egedal, W. Fox, N. Katz, A. Vrublevskis, W. Daughton, and J. F. Drake, *Phys. Plasmas* **17**, 055703 (2010).
- ³⁹M. V. Goldman, G. Lapenta, D. L. Newman, S. Markidis, and H. Che, *Phys. Rev. Lett.* **107**, 135001 (2011).
- ⁴⁰J. Scudder and W. Daughton, *J. Geophys. Res.* **113**, A06222, doi:10.1029/2008JA013035 (2008).
- ⁴¹S. W. H. Cowley and P. Shull, Jr., *Planet. Space Sci.* **31**, 235 (1983).
- ⁴²M. Hoshino, T. Mukai, T. Yamamoto, and S. Kokubun, *J. Geophys. Res.: Space Phys.* **103**, 4509 (1998).
- ⁴³J. T. Gosling, R. M. Skoug, D. J. McComas, and C. W. Smith, *J. Geophys. Res.* **110**, A01107, doi:10.1029/2004JA010809 (2005).
- ⁴⁴J. Buchner and L. Zelenyi, *J. Geophys. Res.* **94**, 11821, doi:10.1029/JA094iA09p11821 (1989).
- ⁴⁵P. D. Hudson, *J. Plasma Phys.* **17**, 419 (1977).
- ⁴⁶H. Karimabadi, D. Krauss-Varban, and N. Omidi, *Geophys. Res. Lett.* **22**, 2689, doi:10.1029/95GL02788 (1995).
- ⁴⁷B. U. Ö. Sonnerup, G. Paschmann, I. Papamastorakis, N. Scopke, G. Haerendel, S. J. Bame, J. R. Asbridge, J. T. Gosling, and C. T. Russell, *J. Geophys. Res.* **86**, 10049, doi:10.1029/JA086iA12p10049 (1981).
- ⁴⁸T.-D. Phan, G. Paschmann, and B. U. Ö. Sonnerup, *J. Geophys. Res.* **101**, 7817, doi:10.1029/95JA03751 (1996).
- ⁴⁹D. Krauss-Varban and N. Omidi, *Geophys. Res. Lett.* **22**, 3271, doi:10.1029/95GL03414 (1995).
- ⁵⁰W. Daughton, V. Roytershteyn, H. Karimabadi, L. Yin, B. J. Albright, B. Bergen, and K. J. Bowers, *Nat. Phys.* **7**, 539 (2011).